

An accurate analytical surface potential model of heterojunction tunnel FET

Yunhe Guan(关云鹤), Huan Li(黎欢), Haifeng Chen(陈海峰), and Siwei Huang(黄思伟)
Citation: Chin. Phys. B, 2023, 32 (**10**): 108506. DOI: 10.1088/1674-1056/accd48
Journal homepage: http://cpb.iphy.ac.cn; http://iopscience.iop.org/cpb

What follows is a list of articles you may be interested in

High on-state current p-type tunnel effect transistor based on doping modulation

Jiale Sun(孙佳乐), Yuming Zhang(张玉明), Hongliang Lu(吕红亮), Zhijun Lyu(吕智军),Yi Zhu(朱翊), Yuche Pan(潘禹澈), and Bin Lu(芦宾)
Chin. Phys. B, 2023, 32 (**7**): 078504. DOI: 10.1088/1674-1056/ac9cbb

Extended-source broken gate tunnel FET for improving direct current and analog/radio-frequency performance

Hui-Fang Xu(许会芳), Wen Sun(孙雯), and Na Wang(王娜)
Chin. Phys. B, 2021, 30 (**7**): 078503. DOI: 10.1088/1674-1056/abe372

haracteristic enhancement in tunnel field-effect transistors via introduction of vertical graded source

Zhijun Lyu(吕智军), Hongliang Lu(吕红亮), Yuming Zhang(张玉明), Yimen Zhang(张义门), Bin Lu(芦宾), Yi Zhu(朱翊), Fankang Meng(孟凡康), Jiale Sun(孙佳乐)
Chin. Phys. B, 2020, 29 (**5**): 058501. DOI: 10.1088/1674-1056/ab7d99

Design and investigation of dopingless double-gate line tunneling transistor: Analog performance, linearity, and harmonic distortion analysis

Hui-Fang Xu(许会芳)†, Xin-Feng Han(韩新风), and Wen Sun(孙雯)
Chin. Phys. B, 2020, 29 (**10**): 108502. DOI: 10.1088/1674-1056/ab9c06

Analysis of non-uniform hetero-gate-dielectric dual-material control gate TFET for suppressing ambipolar nature and improving radio-frequency performance

Hui-Fang Xu(许会芳), Jian Cui(崔健), Wen Sun(孙雯), Xin-Feng Han(韩新风)
Chin. Phys. B, 2019, 28 (**10**): 108501. DOI: 10.1088/1674-1056/ab3a8b

---

An accurate analytical surface potential model of heterojunction tunnel FET

Yunhe Guan(关云鹤)[†], Huan Li(黎欢), Haifeng Chen(陈海峰), and Siwei Huang(黄思伟)

School of Electronic Engineering, Xi'an University of Posts and Telecommunications, Xi'an 710121, *China*

(Received 27 December 2022; revised manuscript received 13 April 2023; accepted manuscript online 16 April 2023)

Based on the accurate and efficient thermal injection method, we develop a fully analytical surface potential model for the heterojunction tunnel field-effect transistor (H-TFET). This model accounts for both the effects of source depletion and inversion charge, which are the key factors influencing the charge, capacitance and current in H-TFET. The accuracy of the model is validated against TCAD simulation and is greatly improved in comparison with the conventional model based on Maxwell–Boltzmann approximation. Furthermore, the dependences of the surface potential and electric field on biases are well predicted and thoroughly analyzed.

Keywords: surface potential model, thermal injection method, tunnel field-effect transistor, heterojunction

PACS: 85.30.De, 85.30.Mn, 85.30.Tv **DOI:** 10.1088/1674-1056/accd48

1. Introduction

Tunnel FETs (TFETs) have been broadly investigated throughout the past decade years because they can deliver $<$ 60 mV/decade subthreshold swing (SS) at room temperature.[1–3] In this way, TFETs are being considered as promising substitutes for MOSFETs in low power applications for future technology nodes. The fabricated III–V heterostructure TFET (H-TFET) with a lateral tunneling junction has demonstrated excellent performance with sub-thermal operation, reaching down to 48 mV/decade, and a high current of 10.6 μA/μm at drain-to-source bias of 0.3 V.[4] The TCAD predicted III–V H-TFET with a trench gate and InGaAs pocket structure achieves simultaneously 921 μA/μm on-current and average subthreshold swing of 4.9 mV/dec.[5]

Despite significant experimental and finite-element simulation efforts,[4–12] an accurate analytical model of the TFET is urgent and indispensable to provide further insight into the physics of the device and to accelerate the process of device and circuit designs. Furthermore, the potential model is the cornerstone of the capacitance and current models,[13,14] which thus needs to be modeled more accurately. In the promising lateral tunneling TFETs, since the tunneling along the interface between the gate oxide and semiconductor or along the surface of the semiconductor is dominant, the surface potential model is more crucial.[14] If there is no specificity, the TFETs discussed later all refer to the kind with a lateral tunneling junction. There have been many reported surface potential models for TFETs.[15–23] Some of these models assume that the channel is depleted,[15,16] which renders them inapplicable when the device is biased in the drain–control region. Although some models take the effect of the inversion charge into account, they ignore the effects of source depletion,[17–19] meaning the models cannot predict the influence of source doping, which is a key parameter to be designed.[20] Both the inversion charge and source depletion have been considered in other surface potential models, but the potential in the channel is derived based on the Maxwell–Boltzmann (M-B) statistics due to its simplicity.[13,21–23] The M-B approximation works well in the MOSFET modeling, but it leads to considerable deviation in the TFET modeling,[17,24] especially for the characteristic in the drain–control region.

In this paper, an accurate analytical surface potential model for the H-TFETs has been developed, which is validated from the linear region to the saturation region. In Section 2, we derive the surface potential model by solving the 2-D Poisson's equation on three regions, i.e., the source/channel depletion regions and the channel transport region, considering the fringing field effect from the gate electrodes and the inversion charge from the drain. Then, the validations of the model against the TCAD simulation are presented in Section 3. At last, the conclusion is drawn in Section 4.

2. Model derivation

Figure 1 describes the schematic structure of the double-gate H-TFET considered in this work. In order to obtain the capacitance or drain current expression, an accurate surface potential profile needs to be derived by solving the pseudo-2-D Poisson's equation first. By TCAD simulation, we get the surface potential profile in the on-state under Fermi–Dirac (F-D) statistics as presented in Fig. 2. In comparison, the surface potential under the M-B statistic is also shown. Note that the channel is within the inversion state, meaning that the device is biased in the drain–control region. It is apparent that the M-B statistic underestimates the surface potential in the chan-

[†]Corresponding author. E-mail: gyhflc@xupt.edu.cn

© 2023 Chinese Physical Society and IOP Publishing Ltd

nel since it overestimates the carrier density (inset of Fig. 2) and thus the voltage drop over the oxide layer. This means that models based on M-B statistics are inappropriate for predicting the surface potential distribution of TFET, and it is an ample necessity to develop a more accurate surface potential model.

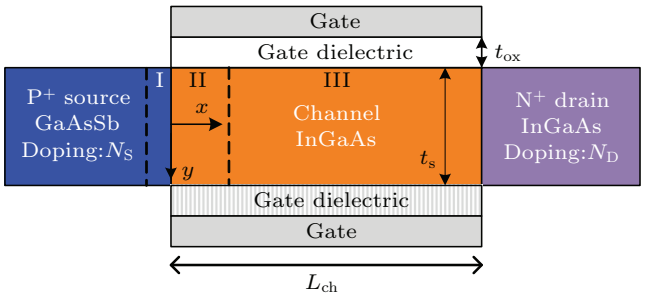


Fig. 1. Schematic cross section of the double-gate heterojunction TFET.

From Fig. 2, the device can be divided into three parts: source depletion region I with length of w_d, channel depletion region II with the length of l_d, and channel transport region III with the surface potential of φ_{ch}. If neglecting the effect of the source depletion region, the surface potential in the entire source region is often assumed to be constant ϕ_{bi} (the built-in potential of the source/channel junction).[19] However, from Fig. 2, it can be seen clearly that the surface potential in region I varies with location and is not a constant. Since the band-to-band tunneling (BTBT) current is highly sensitive to the band bending at the tunnel junction,[19] modeling the surface potential profile in the source depletion region is of importance to improve the accuracy of the proposed model. The surface potential profile in region I $\varphi_{s1}(x)$ is given by[20]

$$\varphi_{s1}(x) = \frac{qN_{S,\mathrm{eff}}}{2\varepsilon_1}(x+w_d)^2+\phi_{bi}, \quad (-w_d \le x < 0), \quad (1)$$

where $N_{S,\mathrm{eff}}$ is the effective source doping considering the fringing field effect,[25,26] ε_1 is the dielectric constant of source material, and $\phi_{bi} = -(\chi_1 + E_{g1} + d_1 - \chi_2 - 0.5E_{g2})/q$, which is defined as the Fermi level difference between the source and channel materials. The degeneracy factor d_1 is given using Fermi integral $F_{1/2}(d_1/kT) = (\pi^{0.5}/2)(N_S/N_V)$ with N_V being the DOS of the source valence band. E_g and χ are the band gap and electron affinity, and the index of 1 and 2 refers to the source and channel material, respectively. q is the electronic charge.

Now, let us observe Fig. 2 again. It can be seen that the surface potential profile in region I obtained by F-D statistics and that by M-B statistics almost coincide although there is an obvious difference between ϕ_{bi} calculated by these two statistics. In region I, the carrier density is very low (inset of Fig. 2), meaning that F-D statistics can be well approximated by M-B statistics and so can the corresponding surface potential. In Eq. (1), in despite of the ϕ_{bi}, i.e., the second part of right-hand side (RHS), the depletion width w_d (in first part of RHS) is also dependent on the chosen statistics. From Fig. 2, w_d (ϕ_{bi}) calculated by F-D statistics is larger (smaller) than that calculated by M-B statistics. Thus, when the F-D statistics is adopted instead of M-B statistics (and vice versa), the influences on these two parts in RHS of Eq. (1) will counteract each other, making the difference inapparent. This also proves the reasonableness of Eq. (1). Moreover, the surface potential profile in region I is very steep with a change of almost 600 meV over a spatial range of about 10 nm, thus the small difference between the F-D and M-B statistics will be further submerged and can hardly be observed.

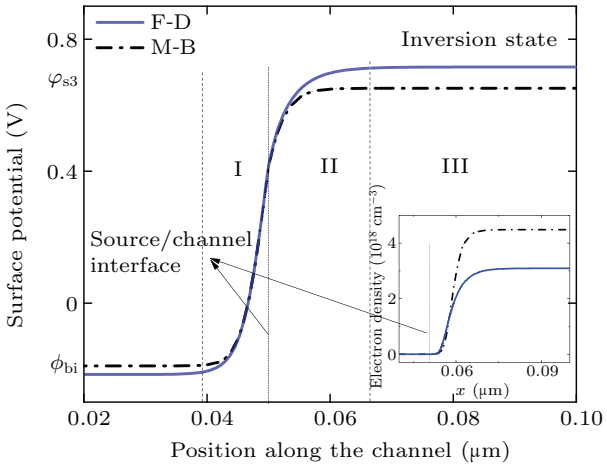


Fig. 2. Surface potential profile of the TFET along the channel under F-D statistic. The case under the M-B statistic is also shown by the dashed dot line. The corresponding electron density along the channel is given in the inset.

Since region II is depleted and the inversion charge can be ignored,[26] and therefore 2-D Poisson's equation can be written as

$$\frac{\partial^2\varphi_2(x,y)}{\partial x^2}+\frac{\partial^2\varphi_2(x,y)}{\partial y^2}=\frac{qN_{CH}}{\varepsilon_2}, \quad (0\le x\le l_d), \quad (2)$$

where $\varphi_2(x,y)$ is the potential distribution, N_{CH} is the channel doping, and ε_2 is the dielectric constant of the channel material. Using the parabolic approximation along the y direction[26,28] and vertical boundary conditions, Eq. (2) can be transformed into a 1-D second-order differential equation

$$\frac{\mathrm{d}^2\varphi_{s2}(x)}{\mathrm{d}x^2}-\frac{\varphi_{s2}(x)}{\lambda^2}=\frac{qN_{CH}}{\varepsilon_2}-\frac{V_{gs}-V_{fb}}{\lambda^2}, \quad (0\le x\le l_d), \quad (3)$$

in which $\varphi_{s2}(x)$ is the surface potential, $\lambda=\sqrt{t_s\varepsilon_s/(2C_{ox})}$ is the characteristic length with $C_{ox}=\varepsilon_{ox}/t_{ox}$ being the gate capacitor per unit area, V_{gs} is the gate voltage, and V_{fb} is the flat-band voltage. By using the boundary conditions at $x=l_d$ (as shown in Fig. 2), i.e., $\mathrm{d}\varphi_{s2}(x)/\mathrm{d}x|_{x=l_d}=0$ and $\varphi_{s2}(l_d)=\varphi_{s3}$, the surface potential in region II is found to be

$$\varphi_{s2}(x)=(\varphi_{s3}-V_{geff})\cosh\left(\frac{x-l_d}{\lambda}\right)+V_{geff}, \quad (0\le x\le l_d) \quad (4)$$

with $V_{\rm geff} = V_{\rm gs} - V_{\rm fb} - \frac{qN_{\rm CH}}{\varepsilon_2}\lambda^2$.

At the boundary between regions I and II, both surface potential and displacement field have to be continuous, which lead to the following two equations:

$$\frac{qN_{\rm S,eff}}{2\varepsilon_1}w_{\rm d}^2 + \phi_{\rm bi} = \left(\varphi_{\rm s3} - V_{\rm geff}\right)\cosh\left(\frac{l_{\rm d}}{\lambda}\right) + V_{\rm geff}, \quad (5)$$

$$qN_{\rm S,eff}w_{\rm d} = \frac{\varepsilon_2}{\lambda}\left(\varphi_{\rm s3} - V_{\rm geff}\right)\sinh\left(\frac{-l_{\rm d}}{\lambda}\right). \quad (6)$$

From Eqs. (5) and (6), $w_{\rm d}$ and $l_{\rm d}$ can be solved as

$$w_{\rm d} = \sqrt{\frac{2\varepsilon_1\varphi_0}{qN_{\rm S,eff}}}, \quad (7)$$

$$l_{\rm d} = \lambda\cosh^{-1}\left(\frac{\varphi_0 + \phi_{\rm bi} - V_{\rm geff}}{\varphi_{\rm s3} - V_{\rm geff}}\right), \quad (8)$$

with

$$\varphi_0 = -\sqrt{\left(V_{\rm geff} - \varphi_{\rm s3}\right)^2 + \phi\left[2\left(V_{\rm geff} - \phi_{\rm bi}\right) + \phi\right]} + V_{\rm geff} - \phi_{\rm bi} + \phi$$

being the value dropping over region I and $\phi = qN_{\rm S,eff}\varepsilon_1\lambda^2/\varepsilon_2^2$. Now, in all the parameters, only the surface potential in region III $\varphi_{\rm s3}$ is unknown.

According to the thermal injection method (TIM),[17] $\varphi_{\rm s3}$ considering the influence of inversion charge can be expressed as (we kindly ask the reader to see more details about the derivation of $\varphi_{\rm s3}$ in Ref. [17])

$$\varphi_{\rm s3} = V_{\rm gs} - V_{\rm fb} - \frac{F_{\rm b}}{2C_{\rm ox}}\left[1 + \frac{C_{\rm ox}}{V_{\rm t}C_{\rm ox} + 0.5F_{\rm b}}\left(V_{\rm gs} - V_{\rm r}\right) + \frac{0.5V_{\rm t}C_{\rm ox}^3}{\left(V_{\rm t}C_{\rm ox} + 0.5F_{\rm b}\right)^3}\left(V_{\rm gs} - V_{\rm r}\right)^2\right], \quad (9)$$

with

$$F_{\rm b} = qt_{\rm s}N_{\rm D}\,{\rm e}^{(V_{\rm r} - d_2 - d_1 - V_{\rm ds})/V_{\rm t}},$$

$$V_{\rm r} = 0.5\left[V_{\rm gs} + V_{\rm cv} - \sqrt{\left(V_{\rm gs} - V_{\rm cv}\right)^2 + \delta^2}\right].$$

$V_{\rm cv} = d_1 + V_{\rm ds} + d_{\rm c}$ is the critical voltage, indicating the transition point between the gate control and drain control, and $d_{\rm c} = kTF_{1/2}^{-1}(0.5N_{\rm inv}\sqrt{\pi}/N_{\rm c})$ is the channel degeneracy factor with screening carrier density $N_{\rm inv}$ and effective density-of-states of conduction band $N_{\rm c}$. $\delta = 0.04$ V is a smoothing factor.

However, it should be noted that at a fixed $V_{\rm ds}$, $\varphi_{\rm s3}$ will decrease with the increase of $V_{\rm gs}$ when $V_{\rm gs}$ is bigger than some values (defined as $V_{\rm gs,max}$) as presented in Fig. 3 (dashed line). This is mathematical but non-physical. Under high gate voltage, the device is within the drain–control region where the surface potential still increases with $V_{\rm gs}$ but very slowly.[19] Thus, for $V_{\rm gs} > V_{\rm gs,max}$, $\varphi_{\rm s3}$ can be approximated to the value at $V_{\rm gs,max}$. By equaling the differentiation of Eq. (9) to 0, $V_{\rm gs,max}$ can be found as

$$V_{\rm gs,max} = V_{\rm cv} + \frac{2\left(V_{\rm t}C_{\rm ox} + 0.5F_{\rm ba}\right)^2}{F_{\rm ba}C_{\rm ox}} \quad (10)$$

with $F_{\rm ba} = qt_{\rm s}N_{\rm D}\,{\rm e}^{(d_{\rm c} - d_2)/V_{\rm t}}$. Note that during the derivation of $V_{\rm gs,max}$, $V_{\rm r}$ is approximated as $V_{\rm cv}$ considering that the $V_{\rm gs}$ around the calculation point is higher. Since this approximation leads to smaller than 0.01% relative error for surface potential (shown in the inset of Fig. 3), indicating that Eq. (10) is reasonable. At this time, the surface potential in region III can be finally written as in Eq. (11), and its changes with $V_{\rm gs}$ are plotted in Fig. 3 (solid line). Now, the dual-modulation effects in TFETs[13,19] are presented well.

$$\varphi_{\rm s3} = \begin{cases} V_{\rm gs} - V_{\rm fb} - \dfrac{F_{\rm b}}{2C_{\rm ox}}\left[1 + \dfrac{C_{\rm ox}}{V_{\rm t}C_{\rm ox} + 0.5F_{\rm b}}\left(V_{\rm gs} - V_{\rm r}\right) + \dfrac{0.5V_{\rm t}C_{\rm ox}^3}{\left(V_{\rm t}C_{\rm ox} + 0.5F_{\rm b}\right)^3}\left(V_{\rm gs} - V_{\rm r}\right)^2\right], & V_{\rm gs} \ll V_{\rm gs,max}, \\ \varphi_{\rm s3}\left(V_{\rm gs,max}\right), & V_{\rm gs} > V_{\rm gs,max}. \end{cases} \quad (11)$$

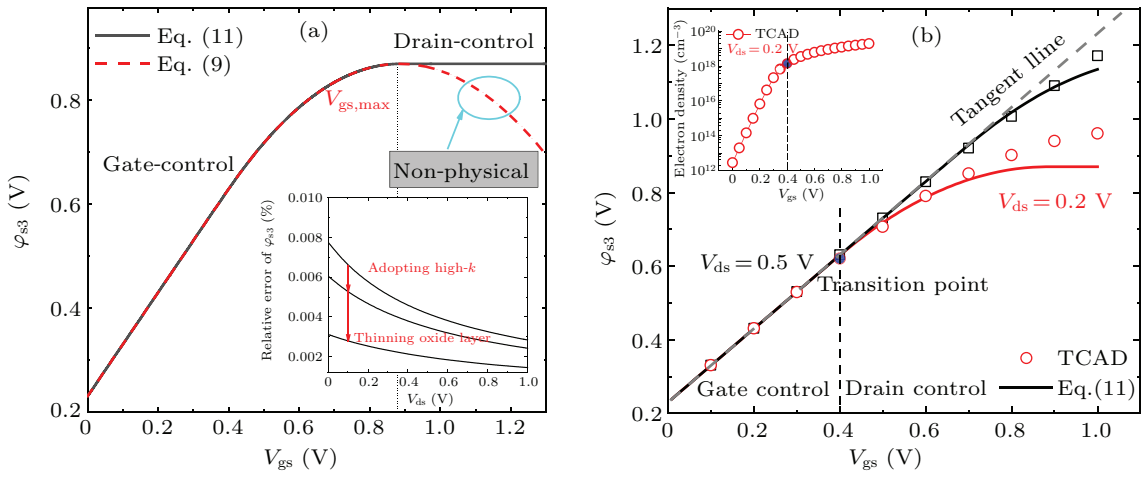


Fig. 3. (a) Surface potential in region III $\varphi_{\rm s3}$ vs. $V_{\rm gs}$ from Eqs. (9) and (11). The inset presents the relative error of surface potential caused by the approximation of $V_{\rm gs,max}$ in Eq. (10). (b) The curves of $\varphi_{\rm s3}$ vs. $V_{\rm gs}$ from Eq. (11) and TCAD simulation under $V_{\rm ds} = 0.2$ V and 0.5 V. The inset shows the curve of inversion electron density vs. $V_{\rm gs}$ under $V_{\rm ds} = 0.2$ V.

3. Model validation

Popular combination with $GaAs_{0.5}Sb_{0.5}/In_{0.53}Ga_{0.47}As$ heterostructure is used because it is not only internally lattice-matched but also lattice matched to the InP substrate.[29] The high-k oxide layer HfO_2 is $t_{ox} = 2$ nm thick with dielectric constant ε_{ox} of 25. The body thickness is $t_s = 10$ nm. The source, channel, and drain regions are p+, p−, and n+ doped, respectively with doping of $N_S = 5 \times 10^{19}$ cm^{-3}, $N_{CH} = 10^{16}$ cm^{-3} and $N_D = 5 \times 10^{18}$ cm^{-3}. The work function of the gate is 4.6 eV.[30] For the numerical simulations of the test TFET, the commercial TCAD tool Sentaurus-device[31] has been used. The dynamic nonlocal tunneling-path method, F-D statistics, and band-gap-narrowing were activated in the simulations. The quantum confinement effects were ignored for the sake of simplicity as in Ref. [26]. The heterojunction interface is assumed to be idealized, because its characteristic would depend on the manufacturing process. Further, the low defect density in the III–V heterojunction has already been demonstrated experimentally through the record high $I_{60} = 0.31$ μA/μm.[4] The parameters for the extraction of the BTBT are taken from Ref. [29], which have been calibrated with the experimental results.

Figure 3(b) shows the dependences of the surface potential in region III φ_{s3} on V_{gs} under different V_{ds}, obtained from the model and TCAD simulation. It can be seen that the model can predict the tendency of φ_{s3} with V_{gs} very well. However, the model underestimates φ_{s3} when V_{gs} is higher, which can be attributed to two aspects: the adopted TIM method and the piecewise function when $V_{gs} \geq V_{gs,max}$. First, it has been demonstrated that the TIM will inevitably underestimate the surface potential when the inversion state is more severe, such as at higher V_{gs} or lower V_{ds},[17] which results from the uniform distribution assumption of the carrier along the y direction used to perform a calculation of φ_{s3}. Second, from the piecewise function when $V_{gs} \geq V_{gs,max}$, φ_{s3} is constant and equal to the value at $V_{gs,max}$, which is inconsistent with the physics. When V_{gs} is high, the surface potential still increases, although slowly[19], which can also be observed from Fig. 3(b). Therefore, the above two reasons should be both in charge of the deviation of φ_{s3} between the results from the model and TCAD at high V_{gs}. From Fig. 3(b), it can also be found that the transition condition between the gate and drain control regions given by the model matches well with that from TCAD simulation. In the drain control region, it has been demonstrated that it is the large amount of inversion electron charge that effectively screens the influence of the gate on surface potential,[19] which can also be illustrated from the inset of Fig. 3(b). This indicates that inversion charge cannot be neglected to predict accurately the performance of TFET, especially when it is biased in the drain control region. Furthermore, in the gate control region, the feature of independence on V_{ds} of φ_{s3}[19] can also be well predicted by the model.

Figure 4(a) presents the dependence of the surface potential in region III on the drain bias from the TCAD simulation and the model under different gate biases. The tendency of φ_{s3} with V_{ds} can be well predicted by the proposed model. When V_{ds} is small, the device is biased in the drain–control region due to the influence of inversion charge, resulting in the φ_{s3} increasing with V_{ds}. However, at the same time, the inversion charge will disappear gradually with the increase of V_{ds}. When there is no inversion charge in the channel eventually, the drain loses the medium to affect the channel surface potential, and the device is biased within the gate-control region. Therefore, φ_{s3} saturates to a value determined by the gate. Meanwhile, the influence of V_{gs} on φ_{s3} can also be predicted from Fig. 4(a). It can also be found that with the increase of V_{ds}, the change rate of φ_{s3} becomes higher and finally equal to that of V_{gs}. For example, when V_{gs} increase from 0.3 V to 0.4 V, the increment of φ_{s3} changes from 70 mV to 100 mV at 0.01 V and 0.25 V of V_{ds}, respectively.

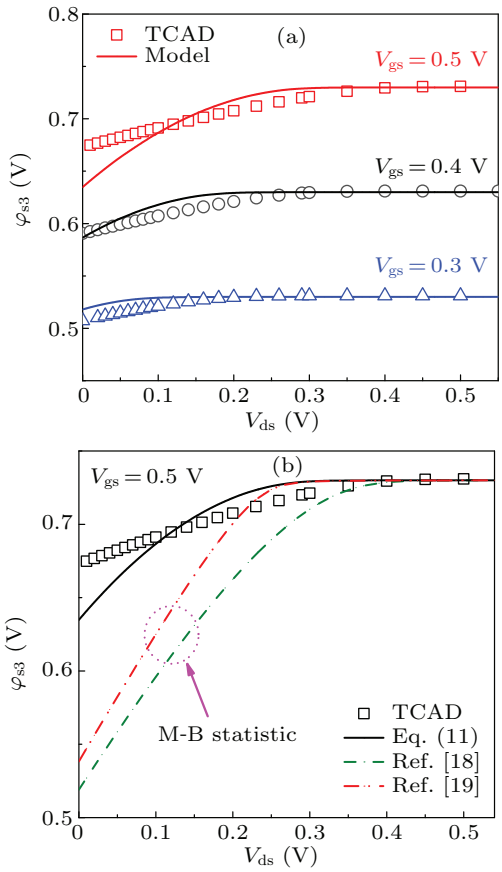


Fig. 4. (a) The dependence of φ_{s3} on V_{ds} under various V_{gs}. (b) The comparison of the φ_{s3}–V_{ds} curves from the proposed model, and the models from Refs. [18,19] under 0.5 V of V_{gs}. Symbols and lines are obtained from TCAD and models, respectively.

The deviation from the model to the TCAD data at small V_{ds} could be attributed to the uniform distribution assumption

of the carrier along the y direction when developing φ_{s3}.[17] As comparisons, the results from the models in Refs. [18,19] are also plotted in Fig. 4(b). Note that these two methods are essentially both based on the M-B statistics. It is apparent that the model based on the adopted TIM is the most accurate to predict the surface potential in the drain control region at a much less computational cost due to that Eq. (11) is fully analytical with no iterative steps. Since the III–V materials, such as InGaAs, have small DOS of the conduction band, severe carrier degeneracy occurs when the inversion layer forms. As presented in Fig. 2, at this time the surface potential from the M-B approximation is lower than that from F-D statistics. Thus, the models from Refs. [18,19], as expected, underestimate the channel surface potential at low V_{ds}. However, the calculation of φ_{s3} in this paper is based on the carrier injection from the drain, and thus evades the inaccuracy problems by the M-B statistics.

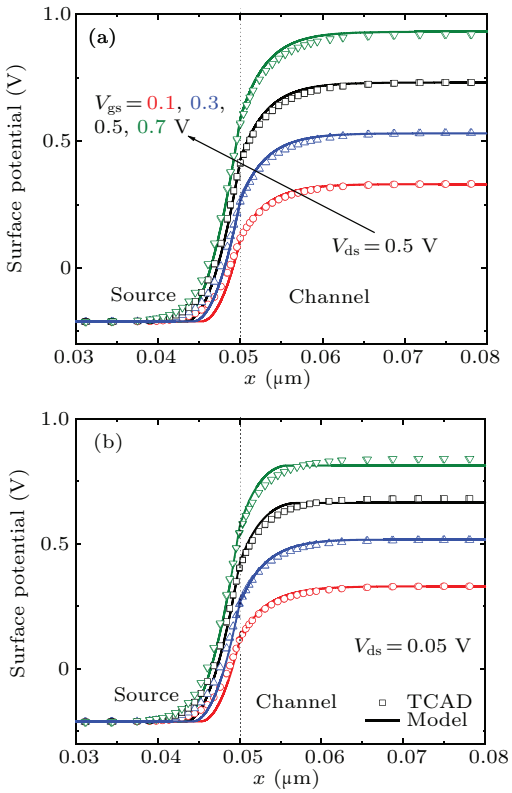


Fig. 5. Surface potential profiles obtained from the model (lines) and TCAD (symbols) under different gate voltages at (a) $V_{ds} = 0.5$ V and (b) $V_{ds} = 0.05$ V.

The surface potential distributions along the channel direction are presented in Fig. 5 under different biases. Good agreement between the model and the TCAD is achieved. The lengths of region I w_d become longer and interface surface potential φ_0 becomes larger with increasing gate voltage because of the effect of the gate fringe field. On the other hand, comparing the plots in Figs. 5(a) and 5(b), it can also be found that the surface potential will increase with drain voltage when the gate voltage is large. For example, at 0.7 V of V_{gs}, the surface potential in the channel is equal to 0.84 V and 0.94 V under $V_{ds} = 0.05$ V and 0.5 V, respectively. The tendency is consistent with the observation shown in Fig. 4.

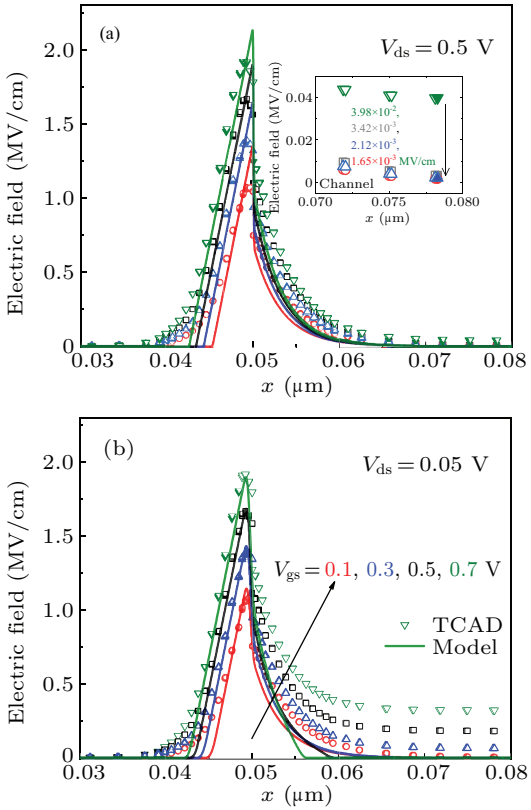


Fig. 6. Electric field profiles obtained from the model (lines) and TCAD (symbols) under different gate voltages at (a) $V_{ds} = 0.5$ V and (b) $V_{ds} = 0.05$ V.

The electric field profiles are shown in Fig. 6 under various biases. The electric field becomes stronger with the increase of V_{gs} due to the steeper surface potential profiles as shown in Fig. 5. The model can also predict the variation of the electric field with biases well. However, it can be observed that there are some mismatches in terms of the maximum value of electric field between the model and the simulation, especially at low V_{gs}. This can be attributed to the assumption used during the model derivation, i.e., the electrical field being zero at the interface of regions II and III. From the enlarged electric field profiles in the channel in the inset of Fig. 6(a), it is obvious that the field is not zero but with small values, indicating that the surface potential predicted by the model is a bit steeper than that from TCAD. Thus, the zero electric field assumption should be responsible for the mismatch of the maximum electric field. However, with the increase of the gate voltage, the mismatch becomes smaller. For example, when V_{gs} increases from 0.1 V to 0.7 V, the relative error of the maximum value between the model and simulation decreases from 28% to 12.5% at 0.5 V of V_{ds}. This is because that the model ignores the vertical part of electric field, which will counteract

the impact of zero electric field assumption. The vertical electric field is induced by the concentration gradient of inversion charge along the y direction as shown in Fig. 7, and it becomes stronger with the increase of V_{gs} due to the higher concentration gradient (Fig. 7). Note that the unit of density gradient is a decade per micrometer. As a result, the model matches very well with the simulation in terms of the maximum electric field at high V_{gs}. Furthermore, the better agreement of the maximum electric field between the model and TCAD under all gate voltages at 0.05 V of V_{ds}, as shown in Fig. 6(b), validates the above explanation. Since at low V_{ds}, the concentration gradient of inversion charge along the y direction remains high even at 0.1 V of V_{gs} (Fig. 7). Although both assuming zero electric field and ignoring the vertical field will lead to the model underestimating the electric field in the channel, the latter is the dominant attributor at low V_{ds} and high V_{gs}. This is further validated in Fig. 8 with lateral ($E_x(x)$), vertical ($E_y(x)$) and total electric field profiles $E_{total}(x)$ from TCAD under 0.05 V of V_{ds} and 0.7 V of V_{gs}. From Fig. 8, it is apparent that it is the vertical part that dominates the electric field in the channel.

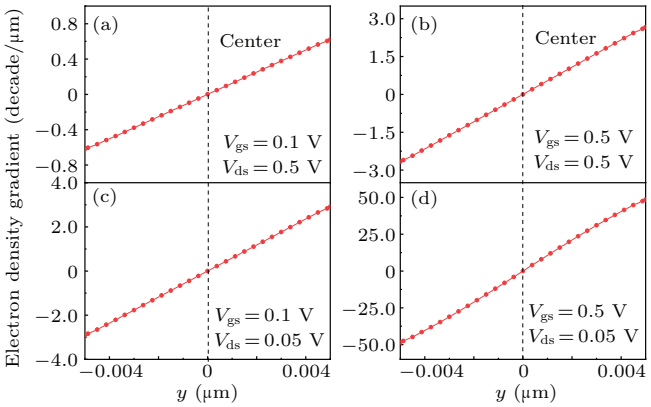


Fig. 7. Electron density gradient profiles along the y direction from TCAD under (a) $V_{gs}=0.1$ V and $V_{ds}=0.5$ V, (b) $V_{gs}=0.5$ V and $V_{ds}=0.5$ V, (c) $V_{gs}=0.1$ V and $V_{ds}=0.05$ V, and (d) $V_{gs}=0.5$ V and $V_{ds}=0.05$ V.

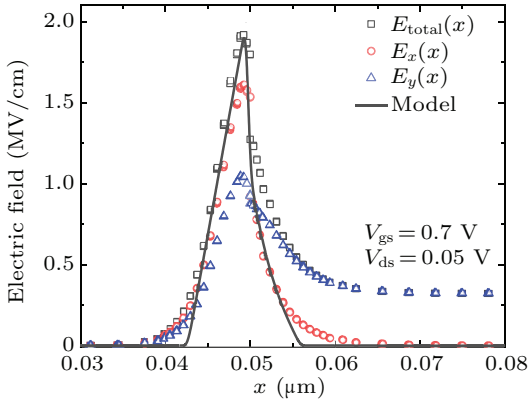


Fig. 8. Total, vertical and lateral electric field profiles along the channel obtained from the TCAD (symbols) under $V_{gs}=0.7$ V and $V_{ds}=0.05$ V.

At last, we want to clarify that the underestimation of the electric field in region II seems not to influence the model to be used in the current derivation based on the simplified Kane expression, since the uniform distribution of the current along the y direction is often assumed[17,21,22,26] which will balance the impact by this mismatch.

4. Conclusion

In this paper, we develop an analytical and accurate surface potential model for the heterojunction TFET based on the thermal injection method. The influences of inversion charge and source depletion are considered. When comparing with the TCAD simulation results, the model predicts the surface potential and electric field profiles under various biases well. Furthermore, the model has obvious superiority over those based on M-B approximation in terms of the accuracy at a much less computational cost when the device is biased within the drain control region due to the adopted thermal injection method. Although, not discussed in detail here, this proposed model can also be used in homojunction TFET or nanowire structures by adjusting the parameters such as built-in voltage and characteristic length.

Acknowledgements

Project supported in part by the National Natural Science Foundation of China (Grant No. 62104192) and in part by the Natural Science Basic Research Program of Shaanxi Province (Grant No. 2021JQ-717).

References

[1] Choi W Y, Park B G, Lee J D and Liu T K 2007 *IEEE Electron Device Lett.* **28** 743
[2] Ionescu A M and Riel H 2011 *Nature* **479** 329
[3] Avci U E and Young I A 2013 *IEEE International Electron Devices Meeting*, December 09–11, 2013, Washington, DC, USA, p. 4.3.1
[4] Memišević E, Hellenbrand M, Lind E, Persson A R, Sant S, Schenk A, Svensson J, Wallenberg R and Wernersson L E 2017 *Nano Lett.* **17** 4373
[5] Chen S, Wang S, Liu H, Han T and Zhang H 2022 *Nanotechnology* **32** 225205
[6] Shao Y and Alamo J A 2022 *IEEE Electron Device Lett.* **43** 846
[7] Li W and Woo J C S 2020 *IEEE Trans. Electron Devices* **67** 1480
[8] Kim H W and Kwon D 2021 *IEEE J. Electron Devices Soc.* **9** 359
[9] Chen Z X, Liu W J, Liu J N, Wang Q H, Zhang X G, Xu J, Li Q H, Bai W and Tang X D 2022 *Chin. Phys. B* **31** 058501
[10] Xu H F, Sun W and Wang N 2021 *Chin. Phys. B* **30** 078503
[11] He Y H, Mao W, Du M, Peng Z L, Wang H Y, Zheng X F, Wang C, Zhang J C and Hao Y 2021 *Chin. Phys. B* **30** 058501
[12] Zhang W H, Li Z C, Guan Y H and Zhang Y F 2017 *Chin. Phys. B* **26** 078502
[13] Jain P, Yadav C, Agarwal A and Chauhan Y S 2017 *Solid-State Electron.* **134** 74
[14] Cheng Q, Khandelwal S and Zeng Y 2022 *IEEE Trans. Electron Devices* **69** 3966
[15] Kumar S, Goel E, Singh K, Singh B, Kumar Singh P, Baral K and Jitl S 2017 *IEEE Trans. Electron Devices* **64** 960
[16] Xu H F, Sun W and Han X F 2018 *Jpn. J. Appl. Phys.* **57** 064201
[17] Guan Y H, Li Z C, Carrillo-Nuñez H, Zhang Y F, Georgiev V P and Asenov A 2019 *IEEE Electron Device Lett.* **40** 1001

[18] Taur Y, Wu J Z and Min J 2015 *IEEE Trans. Electron Devices* **62** 1399
[19] Wu C L, Huang R, Huang Q Q, Wang C, Wang J X and Wang Y Y 2014 *IEEE Trans. Electron Devices* **61** 2690
[20] Min J, Wu J Z and Taur Y 2015 *IEEE Electron Device Lett.* **36** 1094
[21] Lu B, Wang D W, Cui Y, Li Z, Chai G Q, Dong L P, Zhou J R, Wang G L, Miao Y H, Lv Z J and Lu H L 2022 *IEEE Trans. Electron Devices* **69** 419
[22] Mehta J U, Borders W A, Liu H, Pandey R, Datta S and Lunardi L 2016 *IEEE Trans. Electron Devices* **63** 2163
[23] Lu B, Wang D W, Chen Y L, Cui Y, Miao Y H and Dong L P 2021 *Acta Phys. Sin.* **70** 218501 (in Chinese)
[24] Li D, Zhang B L, Lou H J, Zhang L N, Lin X N and Chan M S 2015 *IEEE J. Electron Devices Soc.* **3** 447
[25] Xu W J, Wong H and Iwai H 2015 *Solid-State Electron.* **111** 171
[26] Dong Y P, Zhang L N, Li X B, Lin X N and Chan M S 2016 *IEEE Trans. Electron Devices* **63** 4506
[27] Zhang L N, He J and Chan M S 2012 *International Electron Devices Meeting*, December 10–13, 2012, San Francisco, USA, p. 6.8.1
[28] Guan Y H, Li Z C, Zhang W H, Zhang Y F and Liang F 2018 *IEEE Trans. Electron Devices* **65** 776
[29] Smets Q, Verhulst A S, Kazzi S El, Gundlach D, Richter C A, Mocuta A, Collaert N, Thean A V Y and Heyns M M 2016 *IEEE Trans. Electron Devices* **63** 4248
[30] Choi K M and Choi W Y 2013 *IEEE Electron Device Lett.* **34** 942
[31] TCAD Sentaurus Manual, Synopsys, Inc., Mountain View, CA, USA, 2013